DOI: 10.53469/jpce.2024.06(10).03

Monitoring of Surface Deformation in the Xi'an Coal Mine, Liaoyuan, Based on Time-Series InSAR

Renchao Zhang, Shengwu Qin*, Jiasheng Cao, Yangyang Zhao

College of Construction Engineering, Jilin University, Changchun, China
*Correspondence Author, qinsw@jlu.edu.cn

Abstract: ***In this study, we employed SBAS-InSAR and Stacking-InSAR methods to monitor and analyze the surface deformation of coal mines in the Xi'an District of Liaoyuan. The Pearson correlation coefficient of the deformation results obtained from the two methods is 0.9. Moreover, the deformation regions monitored by the two techniques exhibit a high degree of consistency in their spatial distribution, validating the accuracy of our monitoring results. Using the monitoring data derived from InSAR and field investigations, we revealed the spatial distribution characteristics of surface subsidence and its temporal evolution between 2018 and 2021. Our findings indicate that subsidence predominantly occurred in five regions, with subsidence velocity slowing after October 2020, suggesting a gradual weakening of surface deformation activities. Additionally, we analyzed surface deformation indicators, such as tilt and curvature, revealing the complexity of the deformation areas characterized by multiple tilt and curvature deformation centers. These results provide a crucial scientific basis for geological disaster prevention and ecological restoration in the mining area, aiding the development of more effective management and restoration strategies.***

Keywords: SBAS-InSAR, Stacking-InSAR, Mining Area, Subsidence, Curvature, Inclination.

1. Introduction

The rapid industrialization and urbanization have resulted in significant surface stability issues, particularly in coal mining areas with increasingly severe subsidence problems [*Masood et al., 2020; Schuchová et al., 2020; Zhengfu et al., 2010*]. This subsidence, caused by underground voids from coal extraction, not only threatens the ecological environment and the lives of residents in proximity to mining operations but can also lead to damage of surface infrastructure [*Guzy and Witkowski, 2021; Shongwe, 2018; Younger, 2004*]. Therefore, effective monitoring of mining-induced subsidence is crucial. Traditional subsidence monitoring methods, including leveling surveys, trigonometric leveling, and GNSS monitoring, provide accurate data but are dependent on manually installed monitoring sites [*Shen et al., 2019; Vanicek et al., 1980; Zhou et al., 2013*]. This dependence limits large-scale, high-density monitoring capabilities in mining areas and leads to prohibitively high costs.

Interferometric Synthetic Aperture Radar (InSAR) technology offers distinct advantages in surface deformation monitoring. As a remote sensing technology, InSAR can cover vast areas and provide all-weather, continuous monitoring regardless of weather or lighting, enabling the observation of surface subsidence, landslides, earthquakes, volcanic activity, and other geological hazards [*Aslan, 2019; Cavalié et al., 2008; Perissin et al., 2010; Yang et al., 2016*]. Compared to traditional ground-based methods, InSAR minimizes the need for fieldwork, thus lowering costs and improving efficiency. Additionally, InSAR can integrate with geographic information system (GIS), allowing for a more comprehensive analysis of surface deformation [*Smith, 2002*].

InSAR technology analyzes phase differences between SAR images acquired at different times to generate time series data on surface deformation. It can monitor subtle changes on the Earth's surface with millimeter-level precision, revealing the temporal and spatial development characteristics, trends, and risk levels of subsidence areas [*Jianjun et al., 2017; Lu et al., 2007; Osmanoğlu et al., 2016*]. This information provides a scientific basis for geological disaster prevention and ecological restoration efforts. InSAR technology is divided into two categories: D-InSAR (Differential Synthetic Aperture Radar Interferometry) and Time Series InSAR. D-InSAR compares SAR images from the same area acquired at different times to monitor surface deformation and has been widely used in mining deformation monitoring [*Chen et al., 2021; Hou et al., 2022*]. However, D-InSAR has limitations, such as susceptibility to atmospheric effects, spatial and temporal incoherence, orbital errors, and the inability to retrive time-series deformation. Time-series InSAR overcomes these limitations by analyzing phase information from SAR images over longer periods, allowing for the study of surface deformation trends over time. Time-series InSAR techniques include SBAS-InSAR, Stacking-InSAR and PS-InSAR etc. SBAS-InSAR mitigates spatial and temporal incorrelation by selecting short-baseline interferometric pairs [*Z Li et al., 2019; Osmanoğlu et al., 2016*]. This method requires multilook processing, which sacrifices some image resolution to increase the signal-to-noise ratio of scatterers. The basic principle of Stacking-InSAR is to use multiple SAR images acquired at different times in the same area to reduce atmospheric errors and improve deformation measurement accuracy by stacking phase and amplitude information.

In this paper, the temporal and spatial distribution characteristics of surface subsidence in Liaoyuan Xi'an Coal Mine area are retrived using time-series InSAR technology. Due to the lack of external monitoring data for verification, this study employs SBAS-InSAR as the primary method and Stacking-InSAR for validation. The accuracy of InSAR monitoring results is assessed through a comparison of the two time-series InSAR technologies, alongside field investigation work for validation. Additionally, the spatial and temporal evolution of the subsidence basin and various surface deformation indicators are analyzed.

2. Study Area and Methods

The Liaoyuan Xi'an Coal Mine is located in the northwestern part of Liaoyuan City, Jilin Province, and is recognized as one of the historically significant coal production bases in China (Figure 1). The recoverable coal seam belongs to the Jurassic I coal-bearing stratum, characterized by low ash and low sulfur content, classifying it as high-quality gas coal with a calorific value exceeding 4,500 kcal/kg and an average ash content of 15%. Since the discovery of the coalfield in 1911, Liaoyuan City has undergone over a century of mining activity. Since the 1990s, coal resources have gradually depleted, and by the early 21st century, several coal mining enterprises in the region had declared bankruptcy. Currently, the coal mine is engaged in residual coal extraction, which has led to the emergence of numerous abandoned mine shafts and associated geological hazards such as surface subsidence, resulting in the gradual formation of the Xi'an coal mining subsidence area in Liaoyuan City. According to investigation data, the total area of the subsidence zone is 34.03 square kilometers, of which the ground collapse area is 18.95 square kilometers, while the affected area is 15.08 square kilometers. In recent years, Liaoyuan City has initiated various ecological restoration projects aimed at rehabilitating the geological environment of the coal mining subsidence area. Assessing the distribution of surface subsidence, deformation velocity, and deformation evolution trends in the mining area is significant for the ecological assessment and restoration efforts in this region.

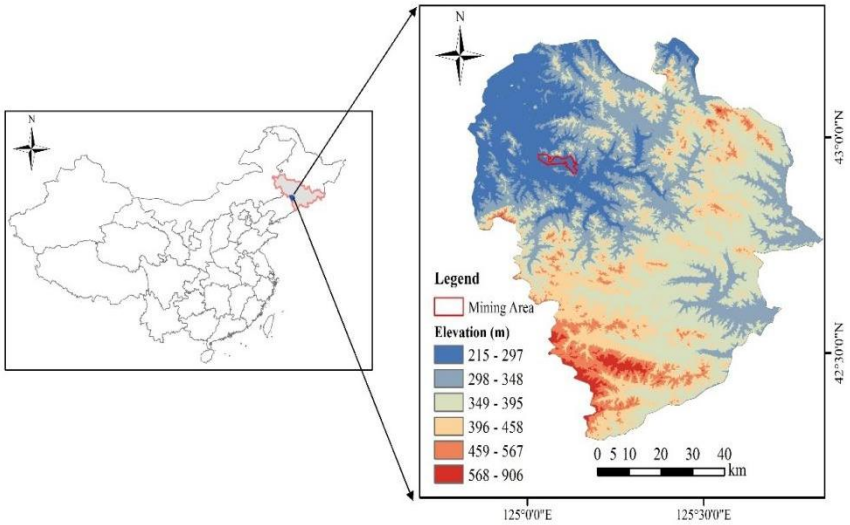

Figure 1: The location of the study area in Xian District, Liaoyuan, Jilin Province, China.

2.1 Data

We download a total of 114 descending Sentinel-1B images acquired between January 6, 2018, and December 1, 2021, to retrieve a long-term surface deformation sequence for the Xi'an coal mining area. The data were collected using VV polarization, specifically with track number 105 and frame number 451 (Table1). The synthetic aperture radar (SAR) images have a resolution of 5×20 m, an incidence angle of 37.90°, and an azimuth angle of 90°. Additionally, we download Precision Orbit Ephemeris (POD) files to correct for orbital errors. The digital elevation model (DEM) with a resolution of 30 meters was also used to co-register the SAR images and remove terrain phase.

Table 1: The Basic Parameters of Sentinel-1B Datasets in the Study Area

Parameter	Data
Direction	Descending
Orbit	105
Frame	451
Resolution	5×20m
Incidence Angle	37.90°
Azimuth Angle	90.00°
Polarization Mode	vv
Quantity	114
Acquisition Time	2018-01-06 – 2021-12-16
Wavelength	5.6cm

2.2 SBAS-InSAR

The Small Baseline Subset (SBAS-InSAR) technique, first introduced by *Berardino et al. [2002]*, enables the retrieval of surface deformation velocities and deformation time-series within a study area, with monitoring accuracy reaching the millimeter level. This method effectively addresses the shortcomings of D-InSAR technology in its applications, significantly improving the precision and reliability of InSAR.

The principle of SBAS-InSAR technology is as follows: assuming that we have acquired a set of SAR images of the study area from t_0 to t_N, setting certain time and spatial thresholds on the data, and then performing interferometry, we obtain M interferometric pairs. The equation that satisfies this condition is as follows:

$$\frac{N+1}{2} < M < \frac{N(N+1)}{2} \quad (1)$$

Perform differential interferometric processing on M pairs of interferometric pairs. Assume the master and slave images for the ith interferometric pair are acquired at times t_B and t_A, respectively. For the jth interferometric pair, the interferometric phase at any point is then expressed as:

$$\Delta\phi_j(x,r) = \phi(t_B,x,r) - \phi(t_A,x,r) \approx \Delta\phi_{disp} + \Delta\phi_{topo} + \Delta\phi_{orb} + \Delta\phi_{atm} + \Delta\phi_{noise} \quad (2)$$

Where $\phi(t_B,x,r)$ and $\phi(t_A,x,r)$ represent the phase of the two images at the point (x,r); $\Delta\phi_{disp}$ denotes the cumulative deformation observed at time t_A and t_B relative to time t_0 along the satellite line of sight. $\Phi_{topo}, \Delta\phi_{orb}, \Delta\phi_{atm}, \Delta\phi_{noise}$ refer to phase errors induced by topography, orbital factors,

atmospheric, and noise.

After removing the deformation errors caused by atmospheric effects, noise, topography, and orbital factors, the phase change can be expressed as:

$$\Delta\phi_j(x,r) = \phi(t_B,x,r) - \phi(t_A,x,r) \approx \frac{4\pi}{\lambda}[d(t_B,x,r) - d(t_A,x,r)] \quad (3)$$

In the equation, $\phi(t_B,x,r)$ and $\phi(t_A,x,r)$ represent the deformation phases, and λ denotes the radar wavelength. Assuming that the initial deformation is zero, the phase time series of the Interferometric can be expressed as:

$$\Phi(t\_I,x,r) = 4\pi/\lambda\ d(t\_I,x,r)(i = 1,\ldots,N) \quad (4)$$

The N unknown phase values corresponding to the deformation at a certain point can be represented as a vector:

$$\Phi = [\phi(t_1),\ldots,\phi(t_N)]^x \quad (5)$$

The vector composed of the phases can be expressed as:

$$\Delta\phi = [\delta\phi_1,\ldots,\delta\phi_M]^x \quad (6)$$

$\delta\phi_i(i = 1,\ldots M)$ is the phase of each point with respect to the reference point. The phase values for the master and slave images can be expressed as:

$$\delta\phi = A\phi \quad (7)$$

A is an M×N matrix, where each row corresponds to an interferometric phase. When the phase is converted to the problem of deformation velocity, it can be converted to:

$$Bv = \delta\phi \quad (8)$$

Where B is the $M \times N$ matrix, the singular value decomposition (SVD) of this matrix allows for the determination of the average velocity v. Subsequently, integration operations can be employed to derive the deformation information for each pixel in the interferometric pairs.

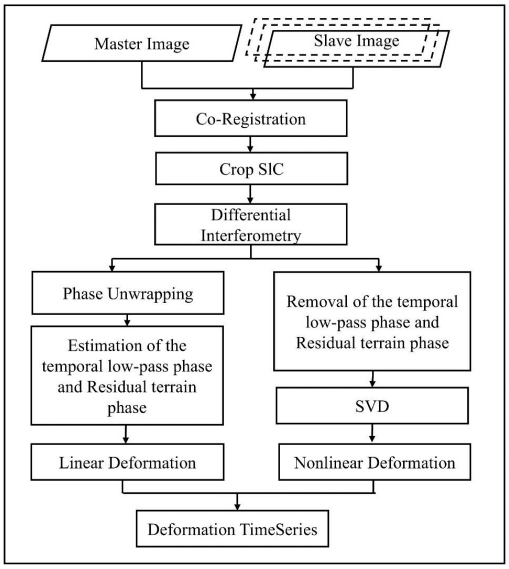

Figure 2: Workflow of SBAS-InSAR technique

2.3 Stacking-InSAR

The Stacking-InSAR technique is employed to obtain linear deformation velocity from a set of Interferometric [*Xu et al., 2022*]. This technique averages the interferometric phases over time, effectively averaging the deformation phases, atmospheric phases, and random noise, thereby providing stronger suppression of atmospheric phase and random noise compared to traditional D-InSAR techniques. The underlying theory is that although atmospheric turbulence disturbances are continuous in the spatial dimension, they are random in the temporal dimension. Therefore, averaging over time effectively suppresses the atmospheric phase. The mathematical model of the Stacking technique is expressed as follows:

$$V_{\text{mean}} = \frac{\sum_{i=1}^{N} \varphi_i \Delta T_i}{\sum_{i=1}^{N} \Delta T_i^2} \quad (9)$$

In the equation, V_{mean} represents the annual average deformation phase velocity, ΔT_I denotes the temporal baseline of the ith Interferometric pair, and φ_I is the unwrapped phase of the ith Interferometric pair. The Stacking-InSAR technique is relatively simple and quick; Its preprocessing steps, including differential interferometric, phase unwrapping, are identical to those of the SBAS-InSAR. The main difference is that Stacking-InSAR calculates deformation by averaging the Interferometric phase.

Due to the lack of measured deformation data in the mining area, this paper uses Stacking-InSAR as validation to verify the accuracy of the SBAS-InSAR results.

2.4 Data Processing

2.4.1 Data Preprocessing

The Sentinel-1B data were processed using the GAMMA software, which was developed by GAMMA Remote Sensing AG company. The SBAS- processing workflow primarily included data preprocessing, differential interferometry, and deformation extraction (Figure 2). During the preprocessing stage, the image from June 24, 2019, was selected as the master image, and other images were resampled and co-registered to this master image. The study area was then cropped to increase computational efficiency.

In the Interferometric processing, the range and azimuth multi-look factors were set to 5:1, the spatial baseline is set to 200 meters and time baseline is set to 80 days when the Interferometric pairs were combined, and a total of 336 pairs are formed (Figure 3).

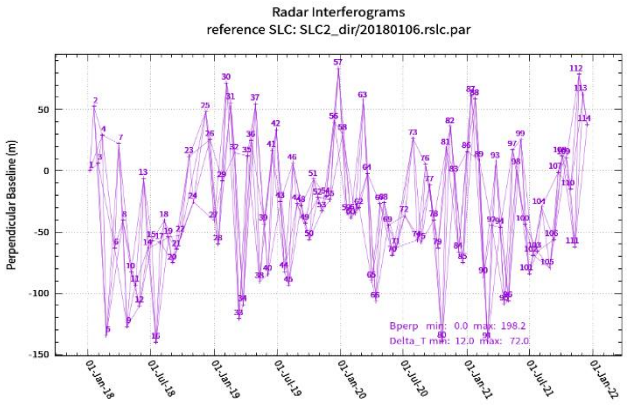

Figure 3: Interconnected network of interferometric pairs.

2.4.2 Interferometric pairs combination and filtering

The coherence in the study area is low due to factors such as vegetation, water, snow, and atmospheric conditions. Consequently, we set a filtering window of size 64 to apply adaptive filtering, which enhances the coherence of the interferometric pairs. The subsequent phase unwrapping process will unwrap the filtered interferometric pairs, establish a coherence threshold, and mask low coherence areas, ensuring they do not contribute to the deformation calculations. This approach prevents errors in unwrapping and deformation analysis caused by low coherence targets. The left side of the information map displays the original interferometric pairs, while the right side presents the filtered interferometric pairs.

The figure shows that, due to the change in surface stress caused by coal extraction, the interferometric graphs generally display circular or elliptical Interferometric fringes (Figure 4). After filtering to remove noise, the distribution of the interferometric phase becomes smoother and more uniform, with the interferometric fringes appearing clearer and more distinct. Additionally, the interferometric circles in 2018 and 2019 are clearer, and the area of the interferometric circles is larger compared to 2020 and 2021. This suggests that the mining area is undergoing continuous subsidence over time. However, between 2020 and 2021, the interferometric circles are smaller, and the interferometric phases are less distinct, suggesting that the velocity of surface subsidence is decreasing.

Subsequently, the interferometric pairs were unwrapped using the minimum cost flow (MCF) algorithm. Finally, the ground deformation parameters for SBAS-InSAR were estimated through Singular Value Decomposition (SVD) on the unwrapped phase, and the deformation velocity of Stacking-InSAR was obtained by averaging the unwrapped phase stacks. After geocoding, the deformation results from SBAS-InSAR and Stacking-InSAR were obtained.

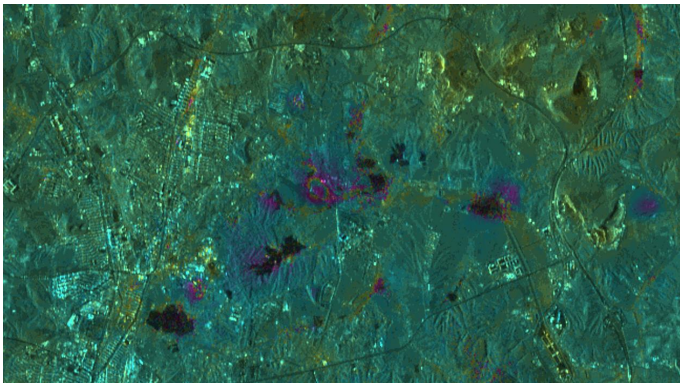

20180118-20180130 (unfiltered)

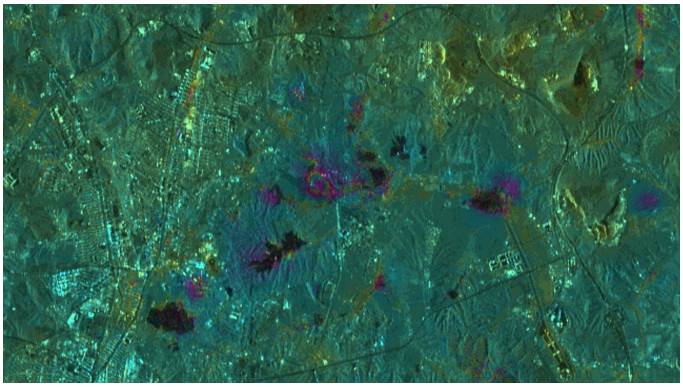

20180118-20180130 (filtered)

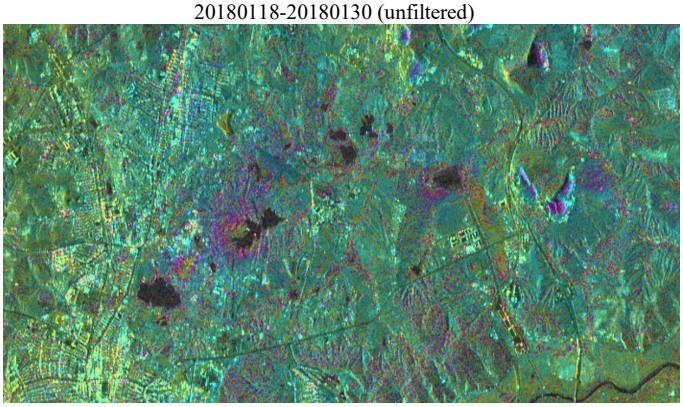

20190113-20190216 (unfiltered)

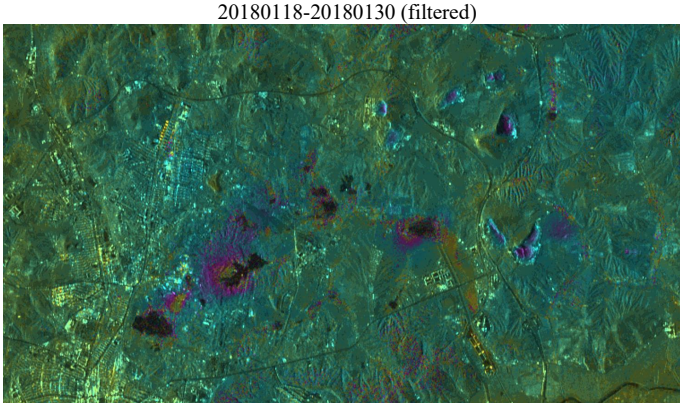

20190113-20190216 (filtered)

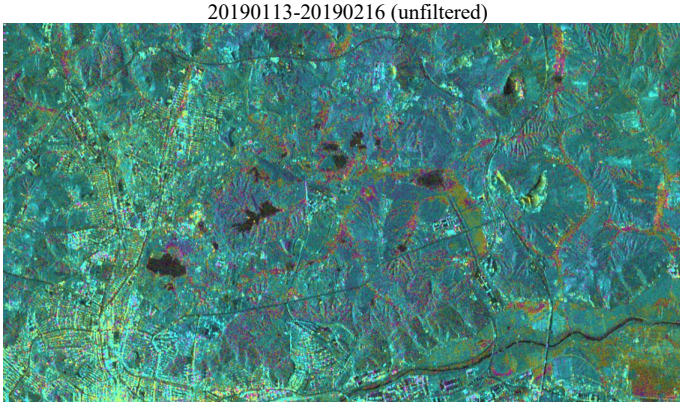

20200108-20200120 (unfiltered)

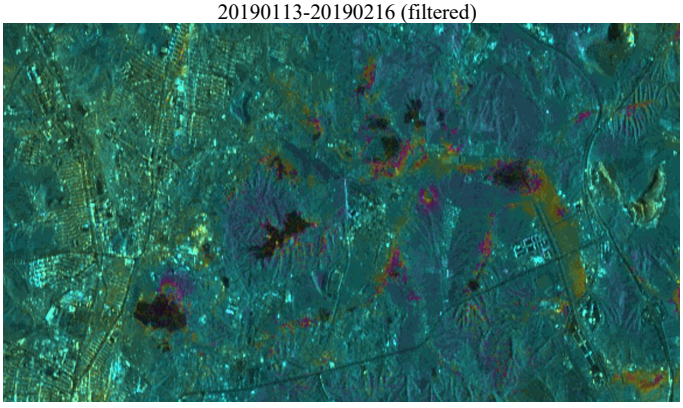

20200108-20200120(filtered)

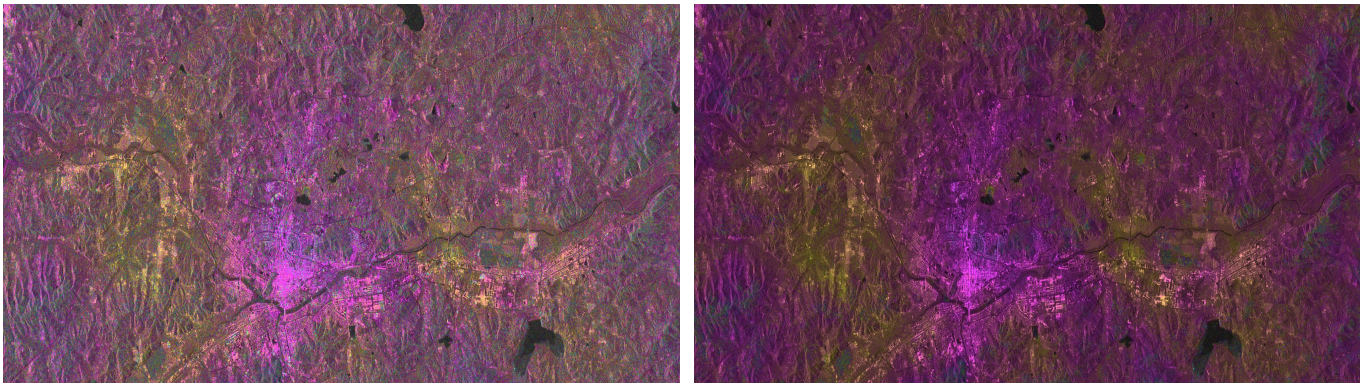

20211017-20211029 (unfiltered) 20211017-20211029 (filtered)

Figure 4: The interferometric pairs from 2018 to 2021, with the unfiltered interferometric pairs on the left and the filtered interferometrich pairs on the right.

3. Results and Disuccsion

Following these steps, the deformation results from SBAS-InSAR and Stacking-InSAR of the Xi'an coal mine were obtained. According to the mining subsidence law, deformation caused by mining mainly manifests as vertical subsidence, with horizontal deformation being significantly smaller [*Behera and Rawat, 2023; G Li et al., 2022; Ścigała et al., 2020*]. Therefore, this paper, assuming negligible horizontal deformation, converts the deformation from the line-of-sight (LOS) direction to the vertical direction.

$$D_V = \frac{D_{Los}}{cos\theta}$$

where D_V is the vertical deformation; D_{Los} is the line-of-sight deformation; θ is the sensor incidence angle.

The monitoring results of SBAS-InSAR and Stacking-InSAR are shown in Figure 5 and Figure 6. The deformation velocity map and cumulative deformation map reveal clear deformation in the mine area between October 2016 and December 2021, which we can classify into five subsidence basins: A, B, C, D, and E. The subsidence areas exhibit a circular or oval distribution. Subsidence area A is located in the western part of the mine, covering 0.37 km², with a subsidence velocity at the center of approximately -53 mm/a. Subsidence area B is located near the middle of the mine boundary, covering 0.81 km², and has a subsidence velocity at the center of about -45 mm/a. Due to long-term, large-scale mining in the southeastern part of the Xi'an mine, surface collapse has occurred, resulting in connected subsidence areas C, D, and E, with a total combined area of about 3 km². The maximum surface subsidence velocity reaches approximately -80 mm/a.

We observed a deficiency in the center of the subsidence funnel monitored by both technologies, primarily due to water accumulation in the large subsidence area caused by mining in the Xi'an coal mine (Figure 5 (c)). Since the surface of the water is typically flat, it reflects radar waves weakly, and natural factors such as wind and waves further affect the signal. This Interferometric significantly alters the coherent signal, making it difficult to obtain sufficient coherence during InSAR analysis. Additionally, the dense vegetation growth in this area, combined with large-scale surface deformation, causes changes in surface scattering characteristics due to vegetation growth and decay, which affects the coherence of SAR images. The decrease in SAR image coherence leads to the loss of phase information, which is a key factor in the loss of subsidence center deformation data.

To further verify our monitoring results, we conducted a field survey of the mining area and identified multiple surface damages caused by coal mining (Figure 6 (a)-(e)). The distribution of observed surface damages (Figure 6 (f)) closely aligns with the surface subsidence distribution patterns monitored by the InSAR technique. We observed numerous collapsed puddles, cracks in roads, damaged houses. The surface damage caused by mining is extensive and severe.

3.1 Accuracy Verification

We extracted the homonymous points from the deformation velocity maps generated by SBAS-InSAR and Stacking-InSAR, subsequently calculating the differences in deformation velocity between these two methods, as illustrated in Figure 7(b). The distribution range of these differences for the homonymous points is approximately [-20 mm/a, 20 mm/a], with a mean value of 0.92mm and a standard deviation of 6.22mm. The differences in deformation velocity between SBAS-inSAR and Stacking-InSAR closely align with characteristics typical of a normal distribution. Notably, the deformation velocity derived from SBAS-InSAR is slightly lower than that obtained through Stacking-InSAR. This discrepancy primarily arises because Stacking-InSAR can only partially mitigate atmospheric noise. By averaging the atmospheric delay phases across interferometric pairs, this technique reduces atmospheric delay effects in deformation results to 1/N of those present in the original image. however, it cannot entirely eliminate their influence. Consequently, some atmospheric phases might be misidentified as deformation phases, which could lead to marginally higher estimates of deformation velocity for Stacking-InSAR.

We conducted a Pearson correlation analysis of the extracted homonymous points (Figure 7(a)), using the deformation velocity obtained from SBAS-InSAR as the x-axis and the deformation velocity from Stacking-InSAR as the y-axis. The correlation coefficient obtained is 0.90. Both methods demonstrate a high degree of consistency regarding the spatial distribution and statistical characteristics, indicating that our monitoring results are accurate.

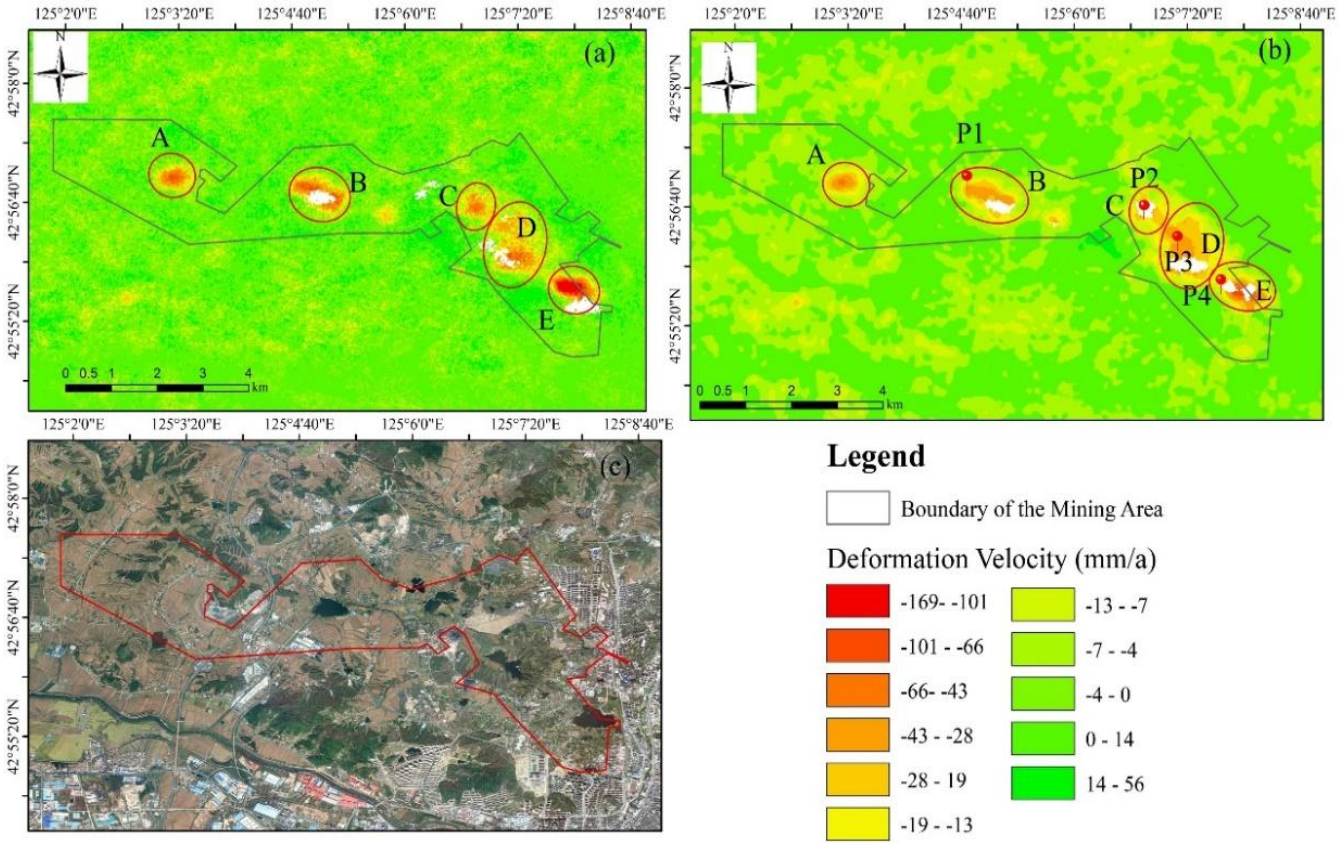

Figure 5: (a) The deformation velocity of Stacking-InSAR; (b) The deformation velocity of SBAS-InSAR, P1, P2, P3, P4 are monitoring points; (c) The Google Earth images of the study area.

Figure 6: (a)-(e) Photographs of some of the ground collapses taken by the field survey work; (f) Locations of ground collapse

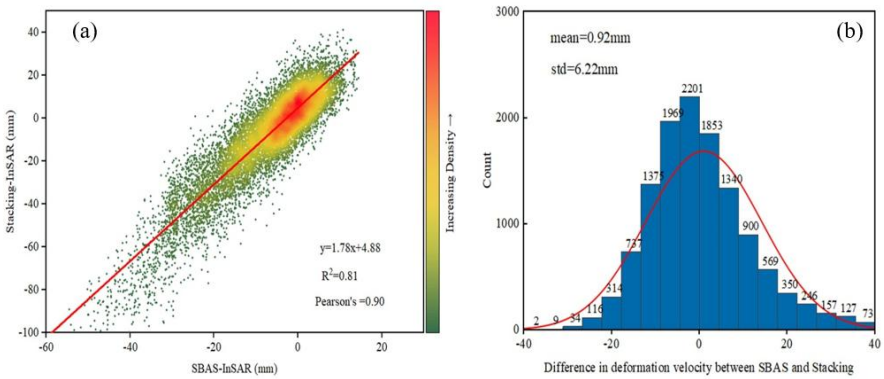

Figure 7: (a) Correlation analysis of SBAS-InSAR and Stacking-InSAR; (b) Distribution of deformation velocity differences at homonymous points between SBAS-InSAR and Stacking-InSAR.

3.2 Analysis of Deformation Evolution Trends in Mining Area

Figure 8 shows the deformation time series obtained from the SBAS-InSAR technique for the Xi'an mining area from January 6, 2018 to December 16, 2021. Each image uses January 6, 2018, as the reference date, assuming that there is no deformation on that date, and it calculates the cumulative deformation for the remaining time periods relative to the reference time, positive values indicate vertical uplift of the ground surface, while negative values indicate vertical subsidence.

From the perspective of deformation evolution, the Xi'an coal mine has continuously experienced subsidence both temporally and spatially. From 2018 to 2020, the surface subsidence area of the mining region exhibited an expansion trend, eventually connecting to the southeastern part of the area to form a large surface collapse zone. After 2021, it is expected that the surface subsidence boundary of the mining region will remain unchanged, although subsidence and deformation continue to some extent.

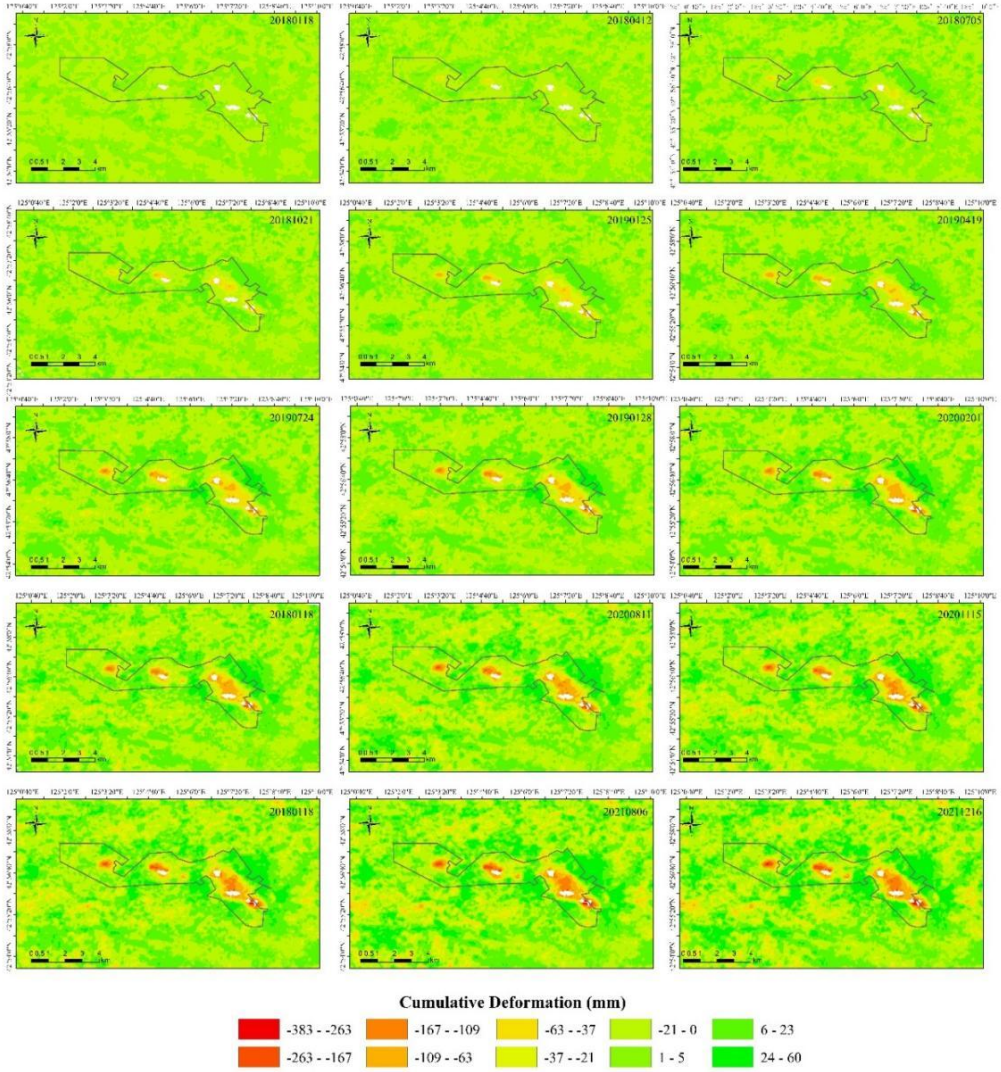

Figure 8: Temporal and spatial evolution of subsidence in Xi 'an Mining area.

After coal seam mining, the surface subsidence will go through start-up stage, active stage and decay stage. The InSAR results are also consistent with the mining surface deformation law, indicating that the mining activities are gradually weakening. We extracted four deformation monitoring points (P1, P2, P3, P4) (Figure 5(b)) to further analyze the evolution process. The cumulative subsidence of points P1, P2, and P3 is approximately 130 mm, with a deformation of about 105 mm from 2018 to October 2020 (Figure 9), corresponding to an annual subsidence of approximately 35 mm. The subsidence during the period from October 2020 to November 2021 is only approximately 25 mm, with a clear deceleration signal. The cumulative subsidence of P4 is about 250mm, and there is only a small subsidence after July 2021. This observation aligns with the change pattern observed in the differential Interferometric from 2018 to 2021(Figure 4).

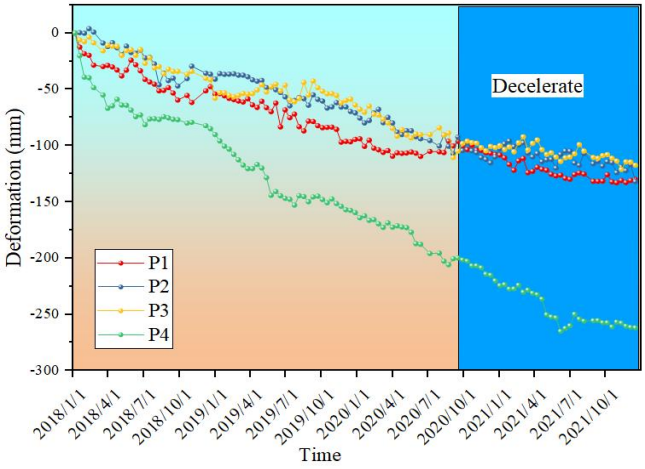

Figure 9: Deformation curves of monitoring points P1, P2, P3, P4.

3.3 Analysis of Deformation Indicators in Mining Areas

In mining subsidence theory, surface movement and deformation are primarily quantified using four indicators: subsidence, tilt, curvature, and horizontal deformation [*Huayang et al., 2002; Kratzsch and Sciences, 1986; Shu et al., 1993*]. Surface subsidence can lead to a reduction in the strength of building foundations, which may adversely affect the usability of the structures. Ground surface tilt can result in a redistribution of base stresses acting on the foundation, potentially compromising the operational condition of machinery and equipment within the building, and in severe cases, causing structural damage and posing risks to personal safety. This issue is particularly pronounced in structures with small base areas and significant heights, such as chimneys and transmission towers. Surface curvature may lead to the formation of seams in buildings.

In this study, the deformation results obtained from InSAR monitoring served as a foundation for further assessing changes in various surface deformation indicators. The NW-SE profiles across the C, D, E area, comprising a total of 18 monitoring points, were extracted and subsequently analyzed for tilt, curvature within the region (Figure 10).

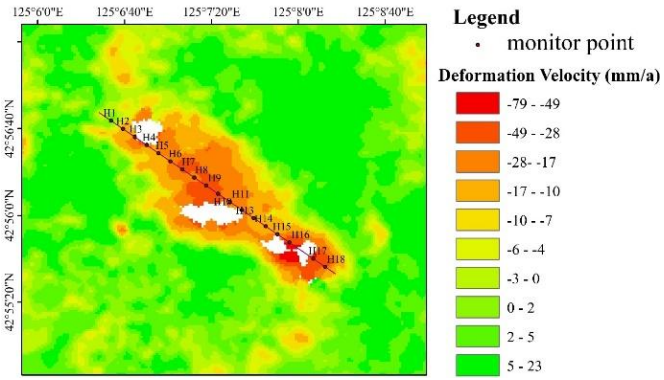

Figure 10: The distribution of the monitoring points along the NW-SE direction.

From the monitoring point H1 to H18, there are multiple subsidence centers located at H3, H7, H10 and H16 (Figure 11). The subsidence funnel at H3 is about 130mm. H7 is the same as H10, and the subsidence in the center of the funnel is about 170mm. The subsidence funnel of H16 is the most obvious, and by December 16, 2021, the cumulative deformation has been about 230mm. It can also be seen from the profile that surface subsidence occurred continuously during the monitoring stage. The deformation was more pronounced in the initial stage and gradually weakened in the later stage.

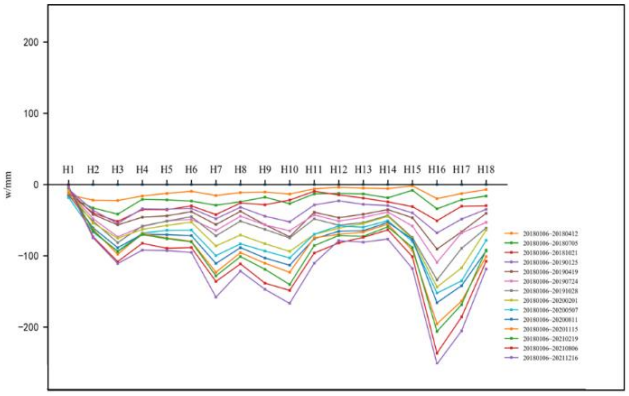

Figure 11: Subsidence time series of NW-SE profile

3.3.1 Inclination

In mining subsidence theory, surface inclination refers to the degree of inclination in a certain direction of the surface subsidence basin, and its calculation formula can be expressed as the ratio of the subsidence difference between adjacent two points and the horizontal distance between these two points:

$$i_k = \frac{W_{k+1} - W_{k-1}}{L} \quad (10)$$

In the formula, i_k is the inclined deformation of surface monitoring point k, W_{k+1}, W_{k-1} is the subsidence value of two points near the monitoring point k and L is the horizontal distance between two points adjacent to the monitoring point k.

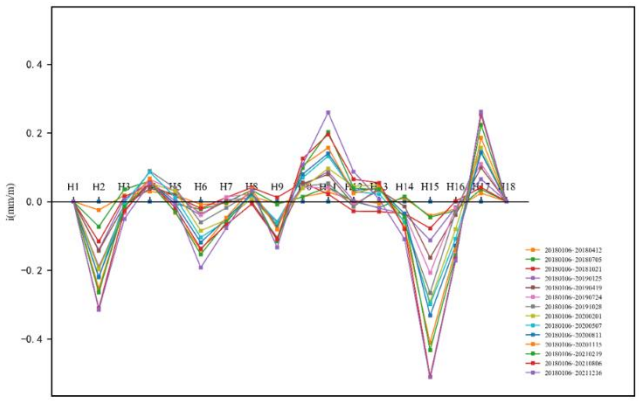

Figure 12: Inclination deformation time series of NW-SE profile.

The positive and negative values of surface inclination indicate the direction of surface deformation. A positive inclination signifies an upward tilt of the surface, while a negative inclination indicates a downward tilt. Analysis of the sequential changes in profile curvature reveals that the surface inclination values continuously increase over time (Figure 12). Like subsidence, the velocity of inclination significantly accelerates during the initial stage and then gradually decelerates in the later stages. Monitoring results of inclination show that there are multiple centers of positive and negative inclination between H1 and H18, including four centers of negative inclination and three centers of positive inclination deformation funnels. The section between H14 and H16 exhibits a significant negative inclination, with the center located near the monitoring point H15, reaching a maximum of -0.5 mm/m. Regarding positive inclination, the amplitudes of inclination are roughly equal for the segments H10-H13 and H16-H18, with a maximum inclination value of approximately 0.3 mm/m.

3.3.2 Curvature

The curvature of the section line within the subsidence basin, which represents the first derivative of the surface inclination i, is denoted as K.

$$K_k = \frac{i_{k+1} - i_{k-1}}{L} \quad (11)$$

In the formula, K_k is the curvature deformation of surface monitoring point k, i_{k+1}, i_{k-1} is the inclination value of two points near the monitoring point k, and L is the horizontal distance between two points adjacent to the monitoring point k.

Surface curvature can be either positive or negative. Positive curvature indicates an upward convex bending of the surface, while negative curvature denotes a downward concave bending. The surface curvature deformation follows a similar pattern to subsidence, with noticeable deformation in the early stages and a gradual reduction in curvature deformation in later stages (Figure 13). Multiple centers of both positive and negative curvature deformation exist. Specifically, the H2-H4, H9-H11, and H15-H17 sections exhibit positive curvature deformation, where the surface shows upward convex bending. In contrast, the H4-H6 and H11-H15 sections display more pronounced downward concave bending. The maximum negative curvature value is approximately -0.0017 mm/m^2, located near monitoring point H14, while the maximum positive curvature value, approximately 0.0017 mm/m^2, is observed at monitoring point H16.

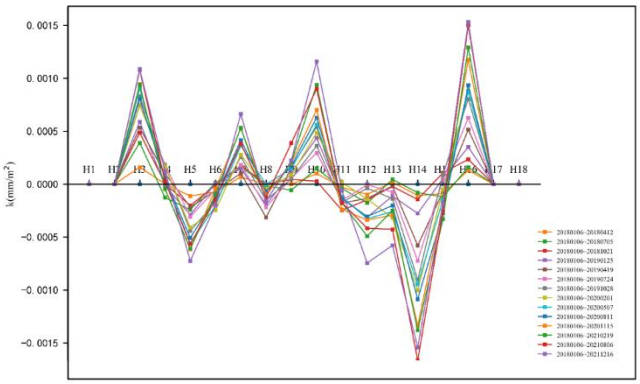

Figure 13: Curvature deformation time series of NW-SE profile.

4. Conclusion:

This study employs time-series InSAR technology to monitor the deformation occurring in the Xi'an coal mining area. By combining field investigations with the analysis of various surface deformation indicators, it maps out the spatial and temporal patterns and progression of deformation within the mined-out area.

(1) We monitored the surface deformation of coal mines in Xi'an District based on two InSAR techniques, SBAS and Stacking, and the cross-validation results showed that the deformation of the mines detected by the two techniques was highly consistent. The Pearson's correlation coefficient reaches 0.9, which proves the accuracy of the InSAR monitoring results. In addition, the field survey work found that there are many house collapses, cracks, and waterlogged sinkholes in the deformation area, which further proves the accuracy of the InSAR detection results.

(2) Based on the interferometric graphs and the time series of surface deformation in the study area, the temporal and spatial evolution characteristics of deformation in the mining area are determined. In the early stage (from 2017 to October 2020), the surface continuously experienced subsidence deformation in time and space. After October 2020, the boundary of the deformation zone basically stopped expanding, and the subsidence velocity slowed down, but it was still slowly occurring subsidence deformation.

(3) A profile in the south-eastern part of the mining area was extracted and analysed for surface deformation indicators. The results show that the surface deformation in the mining area is complex, and there are usually multiple zones of upward and downward tilting deformation on the surface, And multiple upward convex and downward concave curvature deformation zones.

References

[1] Aslan, G. (2019), Monitoring of Surface Deformation In Northwest Turkey From High-Resolution Insar: Focus On Tectonic Aseismic Slip And Subsidence, Université Grenoble Alpes; Istanbul teknik üniversitesi.

[2] Behera, A., and K. S. J. M. T. P. Rawat (2023), A brief review paper on mining subsidence and its geo-environmental impact.
[3] Berardino, P., G. Fornaro, R. Lanari, E. J. I. T. o. g. Sansosti, and r. sensing (2002), A new algorithm for surface deformation monitoring based on small baseline differential SAR Interferometric, 40(11), 2375-2383.
[4] Cavalié, O., C. Lasserre, M.-P. Doin, G. Peltzer, J. Sun, X. Xu, Z.-K. J. E. Shen, and P. S. Letters (2008), Measurement of interseismic strain across the Haiyuan fault (Gansu, China), by InSAR, 275(3-4), 246-257.
[5] Chen, Y., S. Yu, Q. Tao, G. Liu, L. Wang, and F. J. R. S. Wang (2021), Accuracy verification and correction of D-InSAR and SBAS-InSAR in monitoring mining surface subsidence, 13(21), 4365.
[6] Guzy, A., and W. T. J. E. Witkowski (2021), Land subsidence estimation for aquifer drainage induced by underground mining, 14(15), 4658.
[7] Hou, Z., K. Yang, Y. Li, W. Gao, S. Wang, X. Ding, and Y. J. E. e. s. Li (2022), Dynamic prediction model of mining subsidence combined with D-InSAR technical parameter inversion, 81(11), 307.
[8] Huayang, D., W. Jinzhuang, C. Meifeng, W. Lixin, G. J. I. J. o. R. M. Zengzhang, and M. Sciences (2002), Seam dip angle based mining subsidence model and its application, 39(1), 115-123.
[9] Jianjun, Z., L. Zhiwei, and H. J. A. G. e. C. S. Jun (2017), Research progress and methods of InSAR for deformation monitoring, 46(10), 1717.
[10] Kratzsch, I. H. J. E. G., and W. Sciences (1986), Mining subsidence engineering, 8(3), 133-136.
[11] Li, G., Y. Wan, J. Guo, F. Ma, H. Zhao, and Z. J. R. S. Li (2022), A case study on ground subsidence and backfill deformation induced by multi-stage filling mining in a steeply inclined ore body, 14(18), 4555.
[12] Li, Z., Y. Cao, J. Wei, M. Duan, L. Wu, J. Hou, and J. J. E.-S. R. Zhu (2019), Time-series InSAR ground deformation monitoring: Atmospheric delay modeling and estimating, 192, 258-284.
[13] Lu, Z., O. Kwoun, R. J. P. e. Rykhus, and r. sensing (2007), Interferometric synthetic aperture radar (InSAR): its past, present and future, 73(3), 217.
[14] Masood, N., K. Hudson-Edwards, and A. J. J. o. S. M. Farooqi (2020), True cost of coal: Coal mining industry and its associated environmental impacts on water resource development, 19(3), 1.
[15] Osmanoğlu, B., F. Sunar, S. Wdowinski, E. J. I. J. o. P. Cabral-Cano, and R. Sensing (2016), Time series analysis of InSAR data: Methods and trends, 115, 90-102.
[16] Perissin, D., T. J. I. J. o. S. T. i. A. E. O. Wang, and R. Sensing (2010), Time-series InSAR applications over urban areas in China, 4(1), 92-100.
[17] Schuchová, K., J. J. P. i. P. G. E. Lenart, and Environment (2020), Geomorphology of old and abandoned underground mines: Review and future challenges, 44(6), 791-813.
[18] Ścigała, R., K. J. B. o. E. G. Szafulera, and t. Environment (2020), Linear discontinuous deformations created on the surface as an effect of underground mining and local geological conditions-case study, 79(4), 2059-2068.
[19] Shen, N., L. Chen, J. Liu, L. Wang, T. Tao, D. Wu, and R. J. R. S. Chen (2019), A review of global navigation satellite system (GNSS)-based dynamic monitoring technologies for structural health monitoring, 11(9), 1001.
[20] Shongwe, B. N. (2018), The impact of coal mining on the environment and community quality of life: a case study investigation of the impacts and conflicts associated with coal mining in the Mpumalanga Province, South Africa.
[21] Shu, D., A. J. G. Bhattacharyya, and G. Engineering (1993), Prediction of sub-surface subsidence movements due to underground coal mining, 11, 221-234.
[22] Smith, L. C. J. A. o. t. A. o. A. G. (2002), Emerging applications of interferometric synthetic aperture radar (InSAR) in geomorphology and hydrology, 92(3), 385-398.
[23] Vanicek, P., R. O. Castle, and E. I. J. R. o. G. Balazs (1980), Geodetic leveling and its applications, 18(2), 505-524.
[24] Xu, Y., T. Li, X. Tang, X. Zhang, H. Fan, and Y. J. R. S. Wang (2022), Research on the applicability of DInSAR, stacking-InSAR and SBAS-InSAR for mining region subsidence detection in the datong coalfield, 14(14), 3314.
[25] Yang, K., L. Yan, G. Huang, C. Chen, and Z. J. S. Wu (2016), Monitoring building deformation with InSAR: Experiments and validation, 16(12), 2182.
[26] Younger, P. L. J. G. S., London, Special Publications (2004), Environmental impacts of coal mining and associated wastes: a geochemical perspective, 236(1), 169-209.
[27] Zhengfu, B., H. I. Inyang, J. L. Daniels, O. Frank, S. J. M. S. Struthers, and Technology (2010), Environmental issues from coal mining and their solutions, 20(2), 215-223.
[28] Zhou, X. P., M. J. A. M. Sun, and Materials (2013), Study on accuracy measure of trigonometric leveling, 329, 373-377.